

ASSESSMENT OF MODELS OF GALACTIC THERMAL DUST EMISSION USING *COBE*/FIRAS AND *COBE*/DIRBE OBSERVATIONS

N. ODEGARD¹, A. KOGUT², D. T. CHUSS³, N. J. MILLER^{4,2}

Draft version June 29, 2016

ABSTRACT

Accurate modeling of the spectrum of thermal dust emission at millimeter wavelengths is important for improving the accuracy of foreground subtraction for CMB measurements, for improving the accuracy with which the contributions of different foreground emission components can be determined, and for improving our understanding of dust composition and dust physics. We fit four models of dust emission to high Galactic latitude *COBE*/FIRAS and *COBE*/DIRBE observations from 3 millimeters to 100 μ m and compare the quality of the fits. We consider the two-level systems model because it provides a physically motivated explanation for the observed long wavelength flattening of the dust spectrum and the anticorrelation between emissivity index and dust temperature. We consider the model of Finkbeiner, Davis, and Schlegel because it has been widely used for CMB studies, and the generalized version of this model recently applied to *Planck* data by Meisner and Finkbeiner. For comparison we have also fit a phenomenological model consisting of the sum of two graybody components. We find that the two-graybody model gives the best fit and the FDS model gives a significantly poorer fit than the other models. The Meisner and Finkbeiner model and the two-level systems model remain viable for use in Galactic foreground subtraction, but the FIRAS data do not have sufficient signal-to-noise ratio to provide a strong test of the predicted spectrum at millimeter wavelengths.

Subject headings: dust, extinction – infrared: ISM – submillimeter: ISM

1. INTRODUCTION

Diffuse thermal emission from interstellar dust is an important contributor to Galactic foreground emission at millimeter to far-infrared wavelengths. Accurate modeling of its spectrum at these wavelengths is important for studies of the cosmic microwave background (CMB). It is thought to be the dominant contribution to the Galactic foreground at frequencies greater than about 100 GHz (or wavelengths shorter than about 3 millimeters). Contributions from free-free emission, synchrotron emission, and anomalous microwave emission become increasingly important at lower frequencies, and the ratio of CMB anisotropy to Galactic foreground anisotropy peaks at about 70 or 80 GHz for high Galactic latitudes (Bennett et al. 2013, Planck Collaboration 2015 Results X 2015). Improved accuracy in modeling the thermal dust spectrum at millimeter wavelengths is important for improving the accuracy of foreground subtraction for CMB measurements and would allow for more accurate separation of the different foreground component spectra. It would also help our understanding of the composition of dust and the physics of dust emission at these wavelengths.

Observations of the spectrum of Galactic dust show excess emission at submillimeter and millimeter wavelengths relative to a single temperature modified black-

body fit to the far infrared spectrum (e.g. Wright et al. 1991, Reach et al. 1995, Finkbeiner, Davis, and Schlegel 1999, Paradis et al. 2009, Planck Collaboration Int. XVII 2014, Planck Collaboration Int. XXII 2014, Meisner and Finkbeiner 2015). This can be characterized as a flattening of the dust emissivity spectral index β determined from a modified blackbody fit of the form $I_\nu = \tau_{\nu_0}(\nu/\nu_0)^\beta B_\nu(T_d)$, where τ_{ν_0} is the dust optical depth at a reference frequency ν_0 , B_ν is the Planck function and T_d is the dust color temperature. Planck Collaboration Int. XVII (2014) found a flattening $\beta_{FIR} - \beta_{mm}$ of 0.15 for H I correlated dust emission from the diffuse interstellar medium at high Galactic latitude ($b < -25^\circ$), with $\beta_{mm} = 1.53 \pm 0.03$ over $100 \leq \nu \leq 353$ GHz. Planck Collaboration Int. XXII (2014) found a similar result for emission correlated with a 353 GHz dust template at intermediate Galactic latitude ($10^\circ < |b| < 60^\circ$). Using a more recent *Planck* team internal data release, Planck Collaboration Int. XXII (2015) found that band-to-band calibration uncertainties limit the accuracy with which any flattening can be measured.

Some dust emission models account for the submillimeter/millimeter excess by incorporating a cold dust component (e.g., Finkbeiner, Davis, and Schlegel 1999, Meisner and Finkbeiner 2015) or by using optical properties of amorphous silicate dust adjusted to better match the long wavelength observations (e.g., Draine and Li 2007, Compiègne et al. 2011). Other possible mechanisms include long wavelength emission due to low energy excitations in the disordered internal structure of amorphous dust grains (Meny et al. 2007, Paradis et al. 2011), emission from amorphous carbon dust with relatively flat emissivity at long wavelengths (Compiègne et al. 2011, Jones et al. 2013), and magnetic dipole

¹ ADNET Systems, Inc., Code 665, NASA Goddard Space Flight Center, Greenbelt, MD 20771, USA; Nils.Odegard@nasa.gov.

² Code 665, NASA Goddard Space Flight Center, Greenbelt, MD 20771, USA.

³ Department of Physics, Villanova University, 800 E. Lancaster Ave., Villanova, PA, 19085, USA.

⁴ Department of Physics and Astronomy, Johns Hopkins University, 3400 N. Charles St., Baltimore, MD, 21218, USA.

emission from magnetic grains or inclusions (Draine and Hensley 2013).

Many studies have found anticorrelations between dust emissivity spectral index and dust temperature derived from modified blackbody fits at far infrared to millimeter wavelengths (e.g., Dupac et al. 2003, Désert et al. 2008, Paradis et al. 2010, Veneziani et al. 2010, Bracco et al. 2011, Planck Collaboration Early XXIII 2011, Planck Collaboration Early XXV 2011, Kelly et al. 2012, Liang et al. 2012, Juvela et al. 2013, Veneziani et al. 2013, Planck Collaboration Int. XVII 2014, Planck Collaboration 2013 Results XI 2014). Results for the dispersions of β and T_d values and the slope of their correlation vary among different studies; there are differences in sky regions or source samples analysed, differences in datasets and wavelength coverages used, and differences in analysis methods. In many cases it appears that the anticorrelation cannot be explained purely as an effect of measurement uncertainties or fluctuations in the cosmic infrared background, suggesting that it may be an intrinsic characteristic of dust emission. Anticorrelation can also be caused by variations of dust temperature along the line of sight (e.g., Shetty et al. 1996).

Laboratory measurements of interstellar dust analogs at submillimeter to millimeter wavelengths have shown the absorption coefficient spectral index to be anticorrelated with grain temperature for a number of different amorphous grain materials (Agladze et al. 1996, Mennella et al. 1998, Boudet et al. 2005, Coupeaud et al. 2011). For crystalline materials that have been measured, temperature dependence is much weaker or not detected. These results have been interpreted in terms of the two-level systems (TLS) tunneling model for amorphous solids (Phillips 1972, Anderson et al. 1972, Bösch 1978). The TLS model was developed for interstellar dust by Meny et al. (2007) and Paradis et al. (2011). It includes absorption due to acoustic oscillations in a disordered charge distribution (DCD) and absorption due to resonant and relaxation processes in a distribution of low energy two-level tunneling states. The DCD absorption dominates in the far infrared and is temperature independent. Absorption due to hopping relaxation is the largest contributor at millimeter wavelengths and increases with increasing temperature. The hopping relaxation produces long wavelength flattening of the emitted dust spectrum and anticorrelation between emissivity spectral index and temperature. Figure 1 shows the emissivity spectral index predicted by the best-fit TLS model of Paradis et al. (2011) as a function of wavelength and dust temperature.

In this paper, we use *COBE*/FIRAS and *COBE*/DIRBE data to assess the quality of dust emission spectrum predictions from different models in the 100 to 3000 GHz range (3 millimeters to 100 μm). We consider two of the leading physically motivated models, the TLS model because it provides a natural explanation for both the long wavelength flattening of the spectrum and the $\beta - T_d$ anticorrelation, and the model of Finkbeiner, Davis, and Schlegel 1999 (hereafter FDS) because it has been widely used for CMB studies. This model incorporates two dust components with different power-law emissivities that are in equilibrium with the interstellar radiation field. Previous fits of these models have given a reduced χ^2 of 1.85 for a fit of the

FDS model to FIRAS observations (Finkbeiner, Davis, and Schlegel 1999) and a reduced χ^2 of 2.53 for a fit of the TLS model to FIRAS, *WMAP*, and Archeops observations (Paradis et al. 2011). Meisner and Finkbeiner (2015, hereafter MF) obtained a reduced χ^2 of 1.33 from fitting a generalized version of the FDS model with more free parameters to *Planck* High Frequency Instrument (HFI) observations and DIRBE/*IRAS* 100 μm observations.

These results are not directly comparable because of differences in the analyses. Here we make a direct side-by-side comparison of the different models by applying the same analysis method to a common dataset for a common sky region. We compare the fit results for these physical models with those for a purely phenomenological model consisting of the sum of two graybody components. The paper is organized as follows. In §2 we describe the data sets used in the analysis. §3 describes our methods of calculating predictions for the different dust models and fitting them to the data. In §4 we present the fit results and compare them with results of previous studies.

2. DATA SETS

We fit different models of interstellar dust emission to *COBE*/FIRAS and *COBE*/DIRBE data from which estimated contributions of the CMB, cosmic infrared background (CIB), zodiacal light, Galactic synchrotron emission, and Galactic free-free emission have been subtracted. These data sets provide the broad spectral coverage needed to determine the dust model parameters, from the peak dust emission in the far infrared to the Rayleigh-Jeans tail at millimeter wavelengths. Accurate calibration of the FIRAS data was established by interspersing sky measurements with measurements of an external blackbody calibrator that filled the FIRAS beam.

2.1. *COBE*/FIRAS Data

We use data from the final (pass 4) delivery of the FIRAS low spectral resolution Destriped Sky Spectra, which cover 99% of the sky over 213 frequency channels from 68 GHz to 2911 GHz. We subtract the CIB spectrum as determined by Fixsen et al. (1998), $I_\nu^{CIB} = 1.3 \times 10^{-5} (\nu/\nu_0)^{0.64} B_\nu(18.5 \text{ K})$, where $\nu_0 = 3000 \text{ GHz}$. We subtract the publicly released FIRAS zodiacal light model (Brodd et al. 1997), which covers frequencies down to 600 GHz. At lower frequencies where zodiacal emission is not detectable in the FIRAS data, we subtract a power law extrapolation of the model. We subtract Galactic free-free and synchrotron emission using results from *WMAP* 9-year maximum entropy method foreground fitting (Bennett et al. 2013), extrapolated to FIRAS frequencies using a brightness temperature spectral index β of -2.15 for free-free and -3.0 for synchrotron. Free-free and synchrotron emission are negligible compared to the uncertainties in the FIRAS data for the sky regions and frequencies $\nu > 100 \text{ GHz}$ used in our analysis. Anomalous microwave emission is also thought to be negligible at these frequencies (Bennett et al. 2013, Planck Collaboration 2015 Results X 2015) and is not subtracted. We subtract the CMB dipole using the dipole amplitude and direction from *WMAP* (Hinshaw et al. 2009). We used the data with these contributions

subtracted to make an initial fit of each dust emission model as described below but with a CMB monopole component included. The CMB temperature obtained from the initial TLS model fit is 2.72765 K, and the initial FDS and two-graybody fits gave results that agree within 0.00002 K. We subtract this 2.72765 K monopole to obtain the dataset used in our final fit for each dust model. This is consistent with the CMB temperature of 2.728 ± 0.004 K reported by the FIRAS team from analysis of the pass 4 data (Fixsen et al. 1996).

Following FDS, we exclude from our analysis data below 100 GHz due to low signal-to-noise ratio for the dust emission, data above 2100 GHz due to calibration gain uncertainty $\gtrsim 3\%$, and the frequency channels listed in their appendix A due to spectral line emission or problematic data. Our analysis is more susceptible to spectral line contamination than that of FDS, since we do not work with a dataset from which spectral line emission has been fit and subtracted. To take care of line contamination over broader frequency ranges, we also exclude frequency channels 21, 32, 104, 106, 107, 135, 136, 141, and 150. (Following FDS, the numbering here starts at zero for the first channel, at 68 GHz.) This leaves 111 channels in the range $100 \text{ GHz} < \nu < 2100 \text{ GHz}$.

2.2. COBE/DIRBE Data

We use the final (pass 3B) delivery of the DIRBE Zodi-Subtracted Mission Average (ZSMA) sky map at $240 \mu\text{m}$. We subtract the $240 \mu\text{m}$ CIB as determined by Hauser et al. (1998). Instead of using the DIRBE ZSMA map at $100 \mu\text{m}$, we use the $100 \mu\text{m}$ dust emission map of Schlegel, Finkbeiner, and Davis (1998, hereafter SFD) because this map is used in the normalization of the FDS dust model. It was formed by combining DIRBE and *IRAS* $100 \mu\text{m}$ maps, retaining the DIRBE gain and zero point calibration. The *IRAS* data provide measurements of structure at angular scales smaller than the DIRBE beam ($\sim 0.7^\circ$). A DIRBE $25 \mu\text{m}$ template fit was used to subtract zodiacal light and an H I template fit was used to set the zero level of Galactic dust emission. The $100 \mu\text{m}$ and $240 \mu\text{m}$ maps are each smoothed to the FIRAS beam (7° FWHM) and then averaged over FIRAS pixels (2.6° on a side) in the *COBE* quadrilateralized spherical cube projection.

3. ANALYSIS

We fit each dust emission model to the Galactic dust spectra from the FIRAS and DIRBE data. To obtain results characteristic of the diffuse interstellar medium, we use the same mask as that used by FDS to exclude the Galactic plane ($|b| < 7^\circ$), the Magellanic Clouds, and H II regions in Orion and Ophiuchus. The mask also excludes regions that may be affected by FIRAS sidelobe contamination and excludes FIRAS pixels that were not observed or have low weight (weight less than 0.4). The mask excludes 29% of the sky and is shown superposed on a map of FIRAS 1200 GHz ($250 \mu\text{m}$) dust emission in Figure 2. To reduce the time required for our fits to converge, we form mean dust spectra for six large regions covering the sky, with FIRAS pixels inside of the FDS mask excluded. Regions 1 through 4 are 90° wide in Galactic longitude and latitude, centered on the Galactic plane at $l = 0^\circ, 90^\circ, 180^\circ$, and 270° . Regions 5 and 6 are the polar caps at $b < -45^\circ$ and $b > 45^\circ$. For

each region, a weighted mean spectrum is formed using pixel weighting based on the FIRAS detector noise and FIRAS destriper uncertainty β (Brodd et al. 1997). We fit each dust model to the six region-averaged spectra. Table 1 lists the fit parameters that are global and those that vary by region for each dust model.

3.1. Evaluation of the TLS Dust Model

The TLS model is a model of the far-infrared to millimeter wavelength emission from amorphous dust grains, based on a solid-state physics description of the disordered internal structure of the grains (Meny et al. 2007, Paradis et al. 2011). The model includes emission due to acoustic oscillations in the disordered charge distribution (DCD) in the grains and emission by a distribution of localized two-level systems (TLS). Three processes contribute to the two-level systems emission: resonant tunneling, relaxation due to phonon-assisted tunneling, and relaxation due to phonon-assisted hopping. The model is parameterized by (1) the charge correlation length l_c , which determines the wavelength where the spectral index of DCD absorption changes from $\beta = 2$ to $\beta = 4$, (2) the amplitude A of TLS absorption relative to DCD absorption, (3) a parameter of tunneling states, c_Δ , which determines the amplitude of hopping relaxation relative to the other TLS processes, (4) the dust temperature T_d for each sky region, and (5) a scale factor a that sets the overall amplitude of the spectrum for each region. Assuming that l_c , A , and c_Δ are each constant over the sky, Paradis et al. (2011) determined best-fit values for the model parameters using FIRAS and *WMAP* observations of the mean far infrared to millimeter spectral energy distribution of the local interstellar medium, together with Archeops observations of far infrared to submillimeter spectral energy distributions for compact Galactic sources. This showed that the DCD process gives the largest contribution to the total emission at high frequencies and the hopping relaxation process gives the largest contribution below about 170 GHz. Paradis et al. (2012) fit the TLS model to 100–500 μm IRIS and *Herschel* Hi-GAL observations of the inner Galactic plane with l_c and A allowed to vary with position and c_Δ held fixed at the best-fit value from Paradis et al. (2011). Values of A were found to vary significantly in the plane, tracing variations in excess 500 μm emissivity relative to a modified blackbody fit, and no significant variations were found for l_c . On average, A was found to be significantly larger than the best-fit value of Paradis et al. (2011). This was interpreted as due to a higher degree of amorphization of the grains for the inner Galactic plane than for the solar neighborhood. For our TLS model fitting we assume that l_c , A , and c_Δ are each constant over the sky.

We evaluate the predicted spectrum for a given set of parameters following the formulation of Paradis et al. (2011), except we calculate DCD absorption following Bösch (1978). We found that this was necessary to reproduce the predicted DCD, resonant tunneling, and hopping relaxation spectra shown in Figure 2 of Paradis et al. (2011). We have not been able to reproduce the predicted spectra shown for tunneling relaxation, but the contribution of this process to the total spectrum is negligible ($\lesssim 1\%$ for the best-fit parameters of Paradis et al. and the frequency range considered here) so this has no

significant effect on our results.

The predicted spectrum for a given region is calculated as

$$I_\nu(\nu) = a \alpha_{tot}(\nu, T_d, l_c, A, c_\Delta) B_\nu(\nu, T_d), \quad (1)$$

where a is the amplitude scale factor, B_ν is the Planck function, and α_{tot} is the total absorption coefficient given by

$$\alpha_{tot} = \alpha_{DCD} + A(\alpha_{res} + \alpha_{phon} + \alpha_{hop}). \quad (2)$$

We calculate the DCD absorption coefficient following Bösch (1978) as

$$\alpha_{DCD} = \frac{2(\epsilon + 2)^2}{3^3 c \sqrt{\epsilon} v_t^3} \langle \frac{q^2}{m} \rangle \omega^2 \left[1 - \left(1 + \frac{\omega^2}{\omega_0^2} \right)^{-2} \right], \quad (3)$$

where ϵ is the dielectric constant, c is the speed of light, v_t is the transverse sound speed in the material, $\langle \frac{q^2}{m} \rangle$ is the mean squared charge deviation per atomic mass, and $\omega_0 = 2\pi v_t / l_c$ is the characteristic angular frequency where the spectral index of DCD absorption changes from 2 to 4. We use $\epsilon = 2.6$, $v_t = 3 \times 10^5 \text{ cm s}^{-1}$, and $\langle \frac{q^2}{m} \rangle = 6044 \text{ erg cm g}^{-1}$ as used by Bösch (1978) for a soda-lime-silicate glass.

We calculate the absorption coefficients for the TLS processes following Paradis et al. (2011). For resonant tunneling,

$$\alpha_{res} = \frac{4\pi^2}{3c\sqrt{\epsilon}} \frac{(\epsilon + 2)^2}{9} \omega G(\omega) \tanh(\hbar\omega/2kT_d), \quad (4)$$

where $G(\omega)$ is the optical density of states, assumed to be constant at $G(\omega) = G_0 = 1.4 \times 10^{-3}$ in cgs units. This is the value found by Bösch (1978) from fits to absorption measurements of a soda-silicate glass. For phonon-assisted tunneling relaxation,

$$\alpha_{phon} = \frac{G_0}{3c\sqrt{\epsilon}} \frac{(\epsilon + 2)^2}{9} \omega F_2(\omega, T_d), \quad (5)$$

where

$$F_2(\omega, T_d) = \frac{1}{2kT_d} \int_0^\infty \int_{\tau_1}^\infty \sqrt{1 - \frac{\tau_1}{\tau}} \text{sech}^2\left(\frac{E}{2kT_d}\right) \frac{\omega d\tau dE}{1 + \omega^2\tau^2}. \quad (6)$$

Here τ_1 is the relaxation time defined by $\tau_1 = aE^{-3} \tanh(E/2kT_d)$, with a set to $4.2 \times 10^{-56} \text{ erg}^3 \text{ s}$ as found by Bösch (1978) for soda-silica glass. For phonon-assisted hopping relaxation,

$$\alpha_{hop} = \frac{8\pi}{3c\sqrt{\epsilon}} \frac{(\epsilon + 2)^2}{9} G_0(c_\Delta + \ln T_d) \int_0^\infty dV P(V) \frac{\omega^2 \tau}{1 + \omega^2 \tau^2}, \quad (7)$$

where V is the TLS potential energy barrier height and τ is the relaxation time defined by $\tau = \tau_0 \exp(V/T_d)$ with $\tau_0 \simeq 1 \times 10^{-13} \text{ s}$ from Bösch (1978). The tunneling states parameter c_Δ is given by

$$c_\Delta = \ln \frac{k}{\Delta_0^{min}} - 0.441 \quad (8)$$

(Meny et al. 2007) where Δ_0^{min} is the tunnel splitting. The experimental upper limit for Δ_0^{min} corresponds to

$c_\Delta \gtrsim 5.8$. The distribution of TLS barrier height $P(V)$ is approximated as

$$P(V) = \frac{\exp(-(V - V_m)^2/V_0^2)}{V_0\sqrt{\pi}} \quad (9)$$

for $V > V_{min}$ and $P(V) = 0$ for $V < V_{min}$, with $V_{min} = 50 \text{ K}$, $V_m = 550 \text{ K}$, and $V_0 = 410 \text{ K}$ from ultrasonic measurements (Bösch 1978).

Many of the physical parameters adopted for the absorption coefficient calculations are dependent on material characteristics and are not well known for interstellar dust, so the model includes the fit parameter A and also treats c_Δ as a fit parameter.

To obtain model predictions that can be compared with the quoted observations in the DIRBE bands, we apply DIRBE color correction factors based on the predicted spectrum to the model predictions at $100 \mu\text{m}$ and $240 \mu\text{m}$.⁵

3.2. Evaluation of the FDS Dust Model

The best fit model of FDS (their model 8) consists of two dust components, each of which has a power-law emissivity and is in equilibrium with the interstellar radiation field. FDS tentatively identified the colder dust component with amorphous silicate grains and the warmer component with carbonaceous grains. The model is parameterized by the emissivity indices of the cold and warm components, α_1 and α_2 , the fraction of the total emitted power that comes from the cold component, f_1 , and the ratio q_1/q_2 , where q_i is the ratio of the far infrared emission cross section at a reference frequency $\nu_0 = 3000 \text{ GHz}$ to the effective UV-optical absorption cross section for dust component i . Each of these parameters is constant over the sky. For a given set of model parameters, a DIRBE $100 \mu\text{m}/240 \mu\text{m}$ band ratio map is used to determine the temperatures of the two components and the shape of the model spectrum for each map pixel. The SFD $100 \mu\text{m}$ dust emission map determines the amplitude of the model spectrum. FDS determined values for the model parameters by fitting the model to correlation slopes between FIRAS channel maps and the SFD $100 \mu\text{m}$ dust map for the diffuse emission region outside of the mask shown in Figure 2.

We evaluate the FDS model as follows for a given set of model parameters. FDS used the requirement that each dust component is in equilibrium with the interstellar radiation field to obtain a relation between the dust temperatures of the components, T_1 and T_2 ,

$$T_1^{4+\alpha_1} = \frac{q_2 Z(\alpha_2)}{q_1 Z(\alpha_1)} \left(\frac{h\nu_0}{k_B} \right)^{\alpha_1 - \alpha_2} T_2^{4+\alpha_2}, \quad (10)$$

where

$$Z(\alpha) \equiv \int_0^\infty \frac{x^{3+\alpha}}{e^x - 1} dx = \zeta(4 + \alpha) \Gamma(4 + \alpha). \quad (11)$$

We set up a grid of T_2 values varying from 10 to 31 K in steps of 0.1 K and calculate the corresponding values of T_1 . We then calculate values of the DIRBE $100 \mu\text{m}/240 \mu\text{m}$

⁵ DIRBE provided maps of monochromatic brightness at the nominal wavelength for each band assuming that the spectrum νI_ν is constant across the band. For a model spectrum that differs from this, a color correction calculated from the model spectrum and the DIRBE bandpass response function is needed.

μm band ratio R at the grid points using

$$R = \frac{K_{100}(\alpha_1, T_1) f_1 \left(\frac{q_1}{q_2} \right) B_\nu(\nu_{100}, T_1) + K_{100}(\alpha_2, T_2) (1 - f_1) B_\nu(\nu_{100}, T_2)}{K_{240}(\alpha_1, T_1) f_1 \left(\frac{q_1}{q_2} \right) \left(\frac{\nu_{240}}{\nu_{100}} \right)^{\alpha_1} B_\nu(\nu_{240}, T_1) + K_{240}(\alpha_2, T_2) (1 - f_1) \left(\frac{\nu_{240}}{\nu_{100}} \right)^{\alpha_2} B_\nu(\nu_{240}, T_2)}, \quad (12)$$

where K_{100} and K_{240} are color correction factors for the DIRBE 100 μm and 240 μm bands, and ν_{100} and ν_{240} are the nominal frequencies for the DIRBE 100 μm and 240 μm bands.

We use these results with the observed DIRBE 100

$\mu\text{m}/240 \mu\text{m}$ ratio map from FDS to determine T_1 and T_2 for each HEALPix pixel at $N_{\text{side}} = 512$ (pixel size 0.11°). The shape of the predicted spectrum $Y(\nu)$, normalized to the brightness in the DIRBE 100 μm band, is then calculated for each pixel using

$$Y(\nu) = \frac{f_1 \left(\frac{q_1}{q_2} \right) \left(\frac{\nu}{\nu_{100}} \right)^{\alpha_1} B_\nu(\nu, T_1) + (1 - f_1) \left(\frac{\nu}{\nu_{100}} \right)^{\alpha_2} B_\nu(\nu, T_2)}{K_{100}(\alpha_1, T_1) f_1 \left(\frac{q_1}{q_2} \right) B_\nu(\nu_{100}, T_1) + K_{100}(\alpha_2, T_2) (1 - f_1) B_\nu(\nu_{100}, T_2)}, \quad (13)$$

and the predicted spectrum is obtained by multiplying the spectral shape by the brightness from the 100 μm dust emission map made from DIRBE and *IRAS* data by SFD.

We calculate DIRBE 100 μm and 240 μm color correction factors from the model parameters and dust component temperatures, and apply them to the predicted brightness values at ν_{100} and ν_{240} to obtain values that can be compared with the quoted DIRBE observations. The model predictions at each FIRAS frequency and the color-corrected model predictions for each DIRBE band are then smoothed to the FIRAS beam, averaged over FIRAS pixels, and averaged over sky regions using the same pixel weighting as was used for the observed data.

We note some small differences between our analysis and that of FDS. FDS applied a 1% gain recalibration to the FIRAS data to correct for an inconsistency they found between the FIRAS data and the DIRBE 240 μm data. We do not apply any recalibration, but discuss the effect of a possible calibration difference on our results in §4. The SFD 100 μm dust emission map used by FDS is at 0.7° resolution and includes point sources. We use the version at $6'$ resolution with point sources subtracted. The contribution of stars and galaxies is $\lesssim 2\%$ of the Galactic dust emission for the region used in our analysis. There are also small differences in the DIRBE color correction used in the two analyses. The DIRBE Explanatory Supplement tabulates color correction values for modified blackbody spectra over the parameter ranges $0 \leq \beta \leq 2.0$ and $10 \leq T \leq 20000$ K. FDS fit a function to the tabulated values to interpolate and extrapolate in T . We use DIRBE bandpass response functions to calculate the color correction for a given (β, T) . For the 100 μm color correction factor, the method used by FDS generally agrees with the direct calculation within 1% but it underestimates the color correction below 10 K, by as much as 4% for $\beta = 1.67$, $T = 9.0$ K. FDS did not publish their color correction fit coefficients for the 240 μm band.

3.3. Evaluation of the MF Dust Model

We fit the generalized version of the FDS model as formulated by Meisner and Finkbeiner (2015). This version treats one of the dust temperatures, T_2 , and the spectrum amplitude as fit parameters for each region, instead of setting them using the DIRBE 100 $\mu\text{m}/240 \mu\text{m}$ ratio map and the SFD 100 μm dust map. It retains the four global fit parameters of the FDS model ($\alpha_1, \alpha_2, f_1, q_1/q_2$) and the relation between the dust temperatures T_1 and T_2 for each region (equation 10). Meisner and Finkbeiner (2015) fit the model to correlation slopes of *Planck* HFI and DIRBE data relative to *Planck* 857 GHz data for a high Galactic latitude region to determine values for the global parameters, and then made a fit to *Planck* 217, 353, 545, and 857 GHz maps and the SFD 100 μm map at 6.1 arcminute resolution over the entire sky with the global parameter values held fixed. For diffuse sky regions, they found that the model predictions agree with *Planck* 100, 143, and 217 GHz observations within 2.2% on average, and there is similar quality agreement with predictions of the *Planck* team all-sky thermal dust emission model (Planck Collaboration 2013 Results XI 2014) from 353 to 3000 GHz.

The predicted spectrum for this model is given by

$$I_\nu(\nu) = \tau \frac{\left[f_1 \frac{q_1}{q_2} \left(\frac{\nu}{\nu_0} \right)^{\alpha_1} B_\nu(\nu, T_1) + f_2 \left(\frac{\nu}{\nu_0} \right)^{\alpha_2} B_\nu(\nu, T_2) \right]}{\left[f_1 \frac{q_1}{q_2} + f_2 \right]} \quad (14)$$

where τ is the total dust optical depth at a reference frequency ν_0 and $f_2 = 1 - f_1$. We apply DIRBE color correction factors to the 100 μm and 240 μm model predictions to obtain values that can be compared with the quoted DIRBE observations.

3.4. Evaluation of the Two-Graybody Model

We also fit a model consisting of a sum of two modified blackbody components,

$$I_\nu(\nu) = \tau_1 \left(\frac{\nu}{\nu_0} \right)^{\alpha_1} B_\nu(\nu, T_1) + \tau_2 \left(\frac{\nu}{\nu_0} \right)^{\alpha_2} B_\nu(\nu, T_2). \quad (15)$$

Here the parameters τ_1 and τ_2 are optical depths of the two components at a reference frequency ν_0 , which we take to be 1000 GHz, α_1 and α_2 are emissivity indices, and T_1 and T_2 are color temperatures. This is a purely phenomenological model and parameter values from fitting it do not necessarily have any direct physical interpretation. The emissivity indices are taken to be constant over the sky. The temperatures and optical depths may vary from region to region. We have found large degeneracies between parameters if all of them are allowed to be free, so we fix α_1 at 1.7 (close to the best-fit value for component 1 in the FDS model) and solve for the other parameters. We apply DIRBE color correction factors to the 100 μm and 240 μm model predictions to obtain values that can be compared with the quoted DIRBE observations.

3.5. Fit Method

For each model, initial parameter values and parameter covariance matrix are obtained using the Levenberg-Marquardt method to minimize χ^2 calculated using the diagonal of the noise covariance matrix. Final parameter values are obtained using the downhill simplex method of Nelder and Mead (1965) to minimize χ^2 calculated using the full noise covariance matrix,

$$\chi^2 = (\mathbf{I} - \mathbf{M})^T \mathbf{C}^{-1} (\mathbf{I} - \mathbf{M}), \quad (16)$$

where \mathbf{I} is a vector of the observations for all 6 regions and 113 frequencies, \mathbf{M} is a corresponding vector of model predictions, and \mathbf{C}^{-1} is the inverse of the noise covariance matrix.

We include the following FIRAS uncertainties in the noise covariance matrix: detector noise, destriper uncertainty (β), bolometer model gain uncertainty (JCJ gain), calibration model emissivity gain uncertainty (PEP gain), and internal calibrator temperature uncertainty (PUP). These are calculated as described in section 7 of the FIRAS Explanatory Supplement (Brodd et al. 1997). Uncertainty in the absolute temperature scale of the FIRAS external calibrator (PTP) is not included, since it is only important in determination of the absolute temperature of the CMB (Brodd et al. 1997). The DIRBE uncertainties included are absolute calibration gain uncertainty (13.5% at 100 μm and 11.6% at 240 μm) and absolute calibration offset uncertainty. The DIRBE 240 μm uncertainty is much larger than the FIRAS uncertainties at nearby wavelengths, so the DIRBE 240 μm data has little effect on our fit results.

4. RESULTS

Results of our fits of the TLS, FDS, MF, and two-graybody models to the Galactic dust spectra are shown in Figure 3 for a selected region. For the TLS model fit, the DCD process contributes most of the emission above 250 to 300 GHz and hopping relaxation gives the largest contribution at lower frequencies. For the other model fits, the cold dust component gives the largest contribution below about 500 GHz.

Global fit parameters from the model fits are listed in Table 2 and regional fit parameters or regional derived parameters are listed in Table 3. For the FDS model, our fit parameter values are in good agreement (within 2%) with those obtained by FDS for the same sky region from fitting the model to correlation slopes between FIRAS data and 100 μm dust emission. For the MF model, our parameter values are mostly consistent with those obtained by MF for a different, higher Galactic latitude region from fitting the model to correlation slopes of *Planck* HFI and DIRBE data relative to HFI 857 GHz data ($\alpha_1 = 1.63$, $\alpha_2 = 2.82$, $f_1 = 0.0485$, $q_1/q_2 = 8.22$, $T_2 = 15.70$). However, our α_1 value is significantly flatter than that obtained by MF. For the TLS model, our global parameter values are consistent within the uncertainties with the ‘standard’ values of Paradis et al. 2011 ($l_c = 13.40 \pm 1.49$ nm, $A = 5.81 \pm 0.09$, $c_\Delta = 475 \pm 20$) from fitting FIRAS and *WMAP* observations of the diffuse interstellar medium and Archeops observations of compact Galactic sources. Our region-averaged T_{dust} is 18.9 ± 0.3 K, compared with the Paradis et al. standard value 17.26 ± 0.02 K, or 17.53 ± 0.02 K from their fit with the compact source observations excluded. It is not clear if the discrepancy is significant since there are differences in sky coverage. Paradis et al. used FIRAS and *WMAP* data for 14% of the sky where $|b| > 6^\circ$ and $I(240 \mu\text{m}) > 18$ MJy sr $^{-1}$, and we used data for 71% of the sky where $|b| > 7^\circ$ (Figure 2).

We note that the amplitude of the hopping relaxation contribution from our fitting is more accurately determined than would be expected from the large uncertainty in c_Δ given in Table 2. There is a strong degeneracy between c_Δ and A , and the hopping relaxation amplitude is proportional to their product. We estimate the uncertainty in this amplitude to be about 17% from fitting the model with a parameterization that uses a hopping relaxation amplitude parameter instead of c_Δ .

Figure 4 shows a comparison of dust spectra and model fits averaged over the six regions, together with region-averaged fit residuals (dust spectrum minus model fit) and fractional fit residuals. The MF and two-graybody models give a reasonably good fit over the full frequency range, but the TLS and FDS model fits each overpredict the average dust spectrum above about 700 GHz. Figure 5 shows the fractional residual of the different model fits for each region. We note that the difference between the 240 μm DIRBE data points and neighboring FIRAS data points in Figures 4 and 5 is mostly due to calibration differences (Fixsen et al. 1997). The DIRBE 240 μm uncertainty is much larger than the FIRAS uncertainties at nearby wavelengths, so the DIRBE 240 μm data points have little effect on our fit results. The FDS model fit passes straight through the 100 μm data points because the same SFD 100 μm map is used for the model normalization and the data. The FDS model exceeds the 240 μm DIRBE data points because of differences between the FDS 100 μm /240 μm ratio map and the 100 μm /240 μm ratio in the data we are using. This must be due to differences in the methods used in forming the zodiacal light and CIB subtracted map at 240 μm .

Measures of the quality of the model fits are listed in Table 2. Column 3 lists the χ^2 of the fits from equation 15 and column 5 lists the probability of a larger χ^2

value for the number of degrees of freedom ν given in column 4. The FDS model is strongly disfavored compared to the TLS model, and both are worse than the MF and two-graybody models. The two-graybody model gives the best fit because it has the most free parameters for each region. The probability of a larger χ^2 for the two-graybody model is close to unity, indicating that our noise covariance matrix probably overestimates the actual uncertainties somewhat. To get a reduced χ^2 of unity for the two-graybody fit, the uncertainties would need to be decreased by 11%. This would give χ^2_ν values of 1.29, 1.12, and 3.84 and probability of a larger χ^2 of 7×10^{-7} , 0.017, and 2×10^{-266} for the TLS, MF, and FDS fits, respectively.

The TLS, MF, and two-graybody models give acceptable quality fits but the TLS model has very different behavior below 300 GHz where the signal-to-noise ratio of the FIRAS data worsens (Figure 3). The emissivity index of the TLS spectrum continues to flatten with decreasing frequency below 300 GHz. *Planck* data may help to better constrain the different models and differentiate between them at low frequency, or data from future experiments may be needed. From an analysis of a 2014 data release internal to the *Planck* team (release DX11d) together with DIRBE 100 μm data, Planck Collaboration Int. XXII (2015) found that the band-to-band calibration accuracy is not good enough to either confirm or rule out the flattening predicted by the TLS model. The calibration accuracy of the 2015 data release is improved (Planck Collaboration 2015 Results VIII 2015), but the improvement for the 545 GHz and 857 GHz bands is small (5% uncertainty for the 2015 release compared to 7% for DX11d).

In principle, the FDS model might be expected to be better than the others for fitting dust spectra from data averaged over large sky regions since its use of the 100 μm /240 μm ratio map and the 100 μm map allows it to account for variations of dust temperatures and spectrum amplitude on angular scales as small as 1 degree and 6 arcminutes, respectively. However, we find that it gives a poor quality fit because it does not reproduce the large-scale spatial distribution of dust emission as well as the other models do. All of its fit parameters are global, while the other models are free to adjust the amplitude and dust temperature(s) for each region. For the high Galactic latitude regions, Figure 5 shows that the FDS model overpredicts the observations by 10 to 20% over much of the frequency range. Figure 6 shows the residual of the FDS fit calculated at FIRAS resolution ($\sim 7^\circ$ FWHM) and averaged over seven channels centered at 1200 GHz (250 μm). Trends with both Galactic latitude and ecliptic latitude are present, and are also seen in the latitude profiles from the residual map shown in Figure 7.

The ecliptic latitude dependence is probably due to differences between the FIRAS team zodiacal light subtraction, which is based on interpolation and extrapolation of the Kelsall et al. (1998) zodiacal light model to FIRAS frequencies, and the zodiacal light subtraction used in forming the SFD 100 μm map and the FDS 100 μm /240 μm ratio map, which is based on fits to DIRBE 100 μm and 240 μm maps using a DIRBE 25 μm map as a zodiacal light template and an H I map as a Galactic

dust emission template.

The Galactic latitude residual profile is consistent with the corresponding Galactic latitude dust emission profile scaled by 2.8%. This suggests that the Galactic latitude dependence may be a result of inconsistency between the SFD 100 μm map and the FIRAS data due to differences between the DIRBE and FIRAS calibrations. The factor of 2.8% is within the DIRBE 100 μm absolute calibration gain uncertainty of 13.5% and is within the range of DIRBE-FIRAS 100 μm cross-calibration results obtained by Fixsen et al. (1997). Other possible causes for the Galactic latitude dependence include variations in one or more of the model parameters that are taken to be global, or possible systematic errors in the FDS 100 μm /240 μm ratio map at high Galactic latitudes. Such an error in the ratio map could result from errors in the zero levels of the maps it was formed from, due to error in calibration, CIB subtraction, or zodiacal light subtraction. For example, the 1σ uncertainty of the 240 μm CIB from Hauser et al. (1998), which includes calibration and zodiacal light subtraction uncertainties, is about 25% of the mean brightness of the CIB subtracted, zodiacal light subtracted 240 μm data at the Galactic poles.

To see if the FDS model can be modified to reduce the fit residuals, we have tried fitting a modified version of the model that uses the SFD 100 μm map rescaled by 1.028 and a 100 μm /240 μm ratio map calculated from the *Planck* team all-sky thermal dust emission model (Planck Collaboration 2013 Results XI 2014) in place of the FDS ratio map. The *Planck* model was determined from fits of a modified blackbody to *Planck* 353 GHz, 545 GHz, and 857 GHz data with the *Planck* zodiacal emission model subtracted and 100 μm data from a combination of the SFD map at angular scales larger than $30'$ and the IRIS map (Miville-Deschenes and Lagache 2005) at smaller scales. The zero level of each input map was set by correlation with Galactic H I 21-cm line data at low column densities. We used the *Planck* model fit parameters to calculate maps of quoted brightness for the DIRBE 100 μm and 240 μm bands, formed the ratio map, and smoothed it to 1 degree FWHM for use in fitting the modified FDS model. This ratio map has better signal-to-noise ratio than the FDS ratio map, and the maps also differ due to differences in zero levels of the input maps and differences in the zodiacal light subtraction for the 240 μm band. The ratio map from the *Planck* model is systematically larger than the FDS ratio map at high Galactic latitudes, reflecting the increase of the *Planck* model dust temperature with latitude. Figure 7 shows that the modified FDS model fit leads to improvement in both the Galactic latitude profile and the ecliptic latitude profile of the 1200 GHz residual map. The reduced χ^2 of the fit is 1.11, much improved relative to the FDS model fit. This supports the proposition that the FDS model shortcomings in reproducing the spatial distribution of dust emission are mostly due to inconsistency between the DIRBE and FIRAS calibrations and inconsistency between the zodiacal light subtraction, CIB subtraction, and zero-level calibration used for the 100 μm and 240 μm maps and that used for the FIRAS data.

Our fitting does not take into account systematic uncertainties associated with the subtraction of the contributions other than Galactic dust emission from the data. The largest of these uncertainties is in subtraction

of the CIB. We have investigated its effect by making fits where we have increased or decreased the amount of CIB removed by one sigma at all frequencies. We used the one sigma CIB amplitude uncertainties in the FIRAS channels from Fixsen et al. (1998) and the uncertainties in the DIRBE bands from Hauser et al. (1998). The uncertainties are as large as 0.27 MJy sr^{-1} at 1400 GHz. Fitting for the case where the adopted CIB was increased gave significantly poorer fits for the TLS and FDS models and only slightly poorer fits for the MF and two graybody models, with χ^2_ν of 1.71, 7.82, 0.95, and 0.83 for the TLS, FDS, MF, and two graybody fits, respectively. Fitting for the case where the CIB was decreased gave an improved fit for the FDS model and slightly poorer fits for the other models, with χ^2_ν of 1.06, 1.60, 0.93, and 0.85 for the TLS, FDS, MF, and two graybody fits, respectively. In both cases the FDS fit is still significantly worse than the TLS fit, and the dependence of the FDS fit residuals on Galactic latitude and ecliptic latitude is similar to that shown in Figures 6 and 7 for our original FDS fit.

5. SUMMARY AND CONCLUSIONS

We have assessed the quality of fits of the two-level systems, Finkbeiner, Davis, and Schlegel (1999), and Meisner and Finkbeiner (2015) models of thermal dust emission to *COBE*/FIRAS and *COBE*/DIRBE observations of high latitude Galactic dust emission from 100 to 3000 GHz. This is the first side-by-side comparison of these models using a common dataset and a common sky region. For comparison we have also fit a phenomenological model consisting of the sum of two graybody components.

The χ^2 of the fits show that the FDS model is strongly disfavored compared to the other models. It does not reproduce the spatial distribution of dust emission at sub-millimeter wavelengths as well as the other models do. This appears to be mostly due to inconsistency between the DIRBE and FIRAS calibrations and inconsistency

between the zodiacal light subtraction, CIB subtraction, and zero-level calibration used for the 100 μm and 240 μm maps in the FDS model and that used for the FIRAS data. We found big improvement in χ^2 for a modified version of the FDS model that accounts for the apparent inconsistency between the DIRBE and FIRAS calibrations and uses an input 100 μm /240 μm ratio map calculated from the *Planck* team all-sky thermal dust emission model. Variations of the fit residuals with ecliptic latitude and Galactic latitude are significantly reduced. However, the fit is still not quite as good as the fits of the other models, which have freedom to adjust the spectrum amplitude and dust temperature(s) for each sky region.

The Meisner and Finkbeiner model and the TLS model give acceptable quality fits and remain viable physical models for Galactic foreground subtraction in CMB studies. However, the FIRAS data do not provide a strong test of the predicted spectrum below about 300 GHz due to decreasing signal-to-noise ratio. At these frequencies, the TLS model predicts progressive flattening of the spectrum with decreasing frequency that is not predicted by the two-graybody, FDS, or MF models. *Planck* data may help to better constrain different dust models and differentiate between them at low frequency, as will future experiments with large numbers of channels between about 60 and 3000 GHz such as the proposed Primordial Inflation Explorer (PIXIE) mission.

We thank D. Finkbeiner for providing the mask used by FDS, D. Fixsen for helpful discussions about FIRAS data, and D. Paradis for help with questions about the TLS model. We thank the referee for helpful comments. We acknowledge the use of the Legacy Archive for Microwave Background Data Analysis (LAMBDA), part of the High Energy Astrophysics Science Archive Center (HEASARC). HEASARC/LAMBDA is a service of the Astrophysics Science Division at the NASA Goddard Space Flight Center.

REFERENCES

- Agladze, N. I., Sievers, A. J., Jones, S. A., et al. 1996, *ApJ*, 462, 1026
- Anderson, P. W., Halperin, B. I., & Varma, C. M., *Philos. Mag.*, 25, 1
- Bennett, C.L., et al., 2013, *ApJS*, 208, 20B
- Bösch, M.A. 1978, *Phys. Rev. Lett.*, 40, 879
- Boudet, N., Mutschke, H., Nayral, C., et al. 2005, *ApJ*, 633, 272
- Bracco, A., Cooray, A., Veneziani, M., et al. 2011, *MNRAS*, 412, 1151
- Brodd, S., Fixsen, D. J., Jensen, K. A., Mather, J. C., & Shafer, R. A. 1997, *COBE* Far Infrared Absolute Spectrophotometer (FIRAS) Explanatory Supplement, *COBE* Ref. Pub. No. 97-C (Greenbelt, MD: NASA/GSFC), available in electronic form from <http://lambda.gsfc.nasa.gov>
- Compiègne, M., Verstraete, L., Jones, A., et al., 2011, *A&A*, 525, A103
- Coupeaud, A., Demyk, K., Meny, C., et al. 2011, *A&A*, 535, A124
- Désert, F.-X., Macías-Pérez, J. F., Mayet, F., et al. 2008, *A&A*, 481, 411
- Draine, B. T., and Hensley, B., 2013, *ApJ*, 765, 159
- Draine, B. T., and Li, A., 2007, *ApJ*, 657, 810
- Dupac, X., Boudet, N., Giard, M., et al. 2003, *A&A*, 404, L11
- Finkbeiner, D. P., Davis, M., & Schlegel, D. J., 1999, *ApJ*, 524, 867 (FDS)
- Fixsen, D. J., Cheng, E. S., Gales, J. M., et al. 1996, *ApJ*, 473, 576
- Fixsen, D. J., Weiland, J. L., Brodd, S., et al. 1997, *ApJ*, 490, 482
- Fixsen, D. J., Dwek, E., Mather, J. C., Bennett, C. L., & Shafer, R. A. 1998, *ApJ*, 508, 123
- Hauser, M. G., et al. 1998, *ApJ*, 508, 25
- Hinshaw, G., et al. 2009, *ApJS*, 180, 225
- Jones, A. P., Fanciullo, L., Köhler, M., et al., 2013, *A&A*, 558, A62
- Juvela, M., Montillaud, J., Ysard, N., & Lunttila, T. 2013, *A&A*, 556, A63
- Kelly, B. C., Shetty, R., Stutz, A. M., et al. 2012, *ApJ*, 752, 55
- Kelsall, T., et al. 1998, *ApJ*, 508, 44
- Liang, Z., Fixsen, D. J., & Gold, B. 2012, *MNRAS*, submitted (arXiv:1201.0060)
- Meisner, A. M., and Finkbeiner, D. P. 2015, *ApJ*, 798, 88
- Mennella, V., Brucato, J. R., Colangeli, L., et al. 1998, *ApJ*, 496, 1058
- Meny, C., Gromov, V., Boudet, N., Bernard, J.-Ph., Paradis, D., & Nayral, C. 2007, *A&A*, 468, 171
- Miville-Deschenes, M.-A. & Lagache, G. 2005, *ApJS*, 157, 302
- Nelder, J. A., & Mead, R. 1965, *Computer Journal*, 7, 308
- Paradis, D., Bernard, J.-Ph., & Mény, C. 2009, *A&A*, 506, 745
- Paradis, D., Bernard, J.-Ph., Mény, C., & Gromov, V. 2011, *A&A*, 534, 118
- Paradis, D., Paladini, R., Noriega-Crespo, A., et al. 2012, *A&A*, 537, A113
- Paradis, D., Veneziani, M., Noriega-Crespo, A., et al. 2010, *A&A*, 520, L8
- Phillips, W. A. 1972, *J. Low Temp. Phys.*, 7, 351
- Planck Collaboration Early XXIII, Ade, P. A. R., Aghanim, N., Arnaud, M., et al. 2011, *A&A*, 536, A23
- Planck Collaboration Early XXV, Abergel, A., Ade, P. A. R., Aghanim, N., et al. 2011, *A&A*, 536, A25

- Planck Collaboration Int. XVII, Abergel, A., Ade, P. A. R., Aghanim, N., Alves, M. I. R., et al., 2014, *A&A*, 566, 55
- Planck Collaboration Int. XXII, Ade, P. A. R., Alves, M. I. R., Aniano, G., Armitage-Caplan, C., et al. 2015, *A&A*, 576, A107
- Planck Collaboration 2013 Results XI, Abergel, A., Ade, P. A. R., Aghanim, N., et al. 2014, *A&A*, 571, A11
- Planck Collaboration 2015 Results VIII, Adam, R., Ade, P. A. R., Aghanim, N., et al. 2015, *A&A*, submitted (arXiv:1502.01587)
- Planck Collaboration 2015 Results X, Adam, R., Ade, P. A. R., Aghanim, N., et al. 2015, *A&A*, submitted (arXiv:1502.01588)
- Reach, W. T., Dwek, E., Fixsen, D. J., et al., 1995, *ApJ*, 451, 188
- Schlegel, D. J., Finkbeiner, D. P., & Davis, M. 1998, *ApJ*, 500, 525 (SFD)
- Shetty, R. Kauffmann, J., Schnee, S., et al. 1996, *ApJ*, 696, 2234
- Veneziani, M., Ade, P. A. R., Bock, J. J., et al. 2010, *ApJ*, 713, 959
- Veneziani, M., Piacentini, F., Noriega-Crespo, A., et al. 2013, *ApJ*, 772, 56
- Wright, E. L., Mather, J. C., Bennett, C. L., et al., 1991, *ApJ*, 381, 200

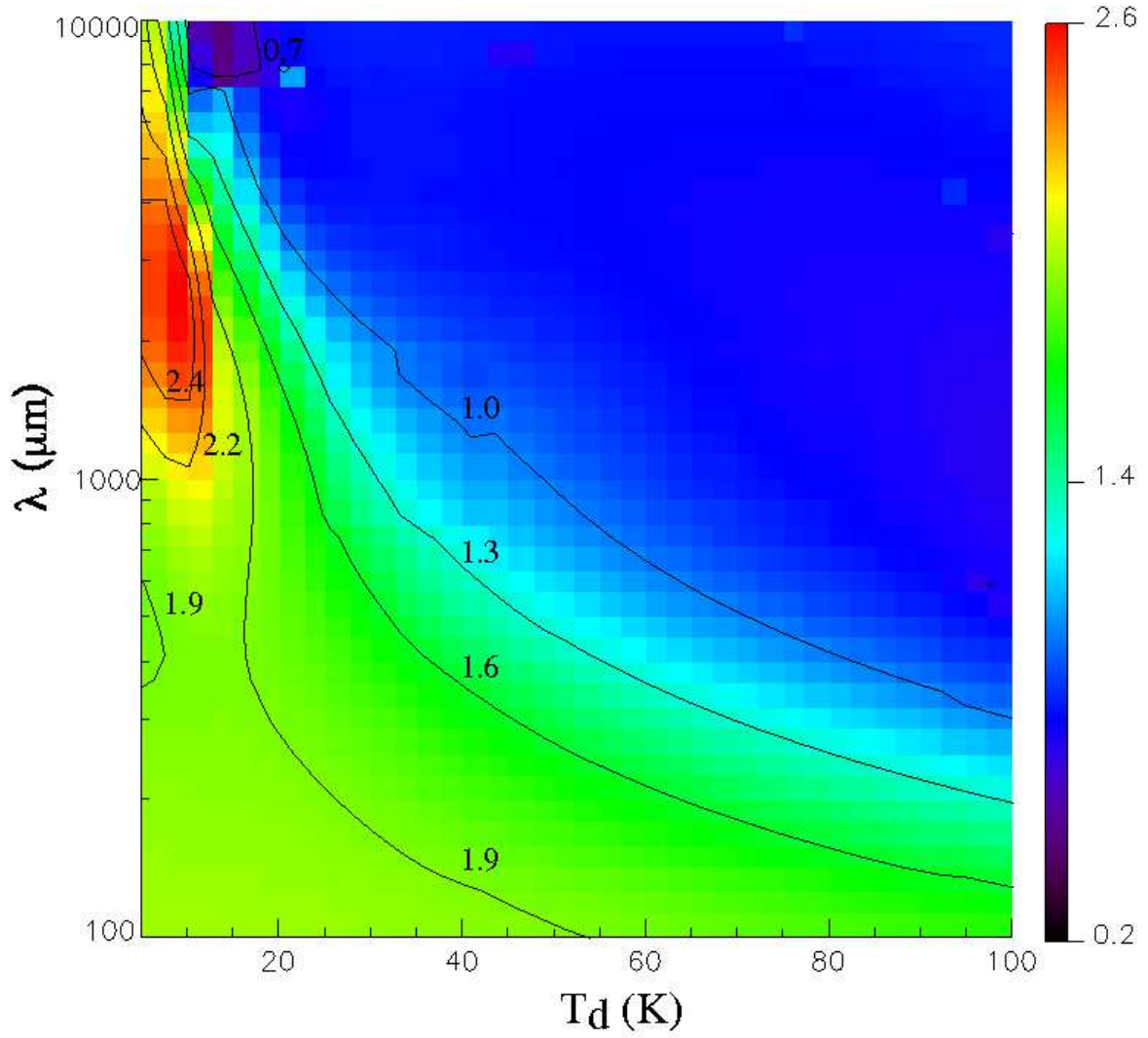


Figure 1. The dust emissivity spectral index predicted by the two-level systems model as a function of wavelength and dust temperature. This figure is from Paradis et al. (2011) and is based on their best-fit model parameters. The model provides a natural explanation for both the observed long wavelength flattening of the spectrum and the anticorrelation between emissivity spectral index and dust temperature. Credit: Paradis et al., A&A, 534, 118, 2011, reproduced with permission ©ESO.

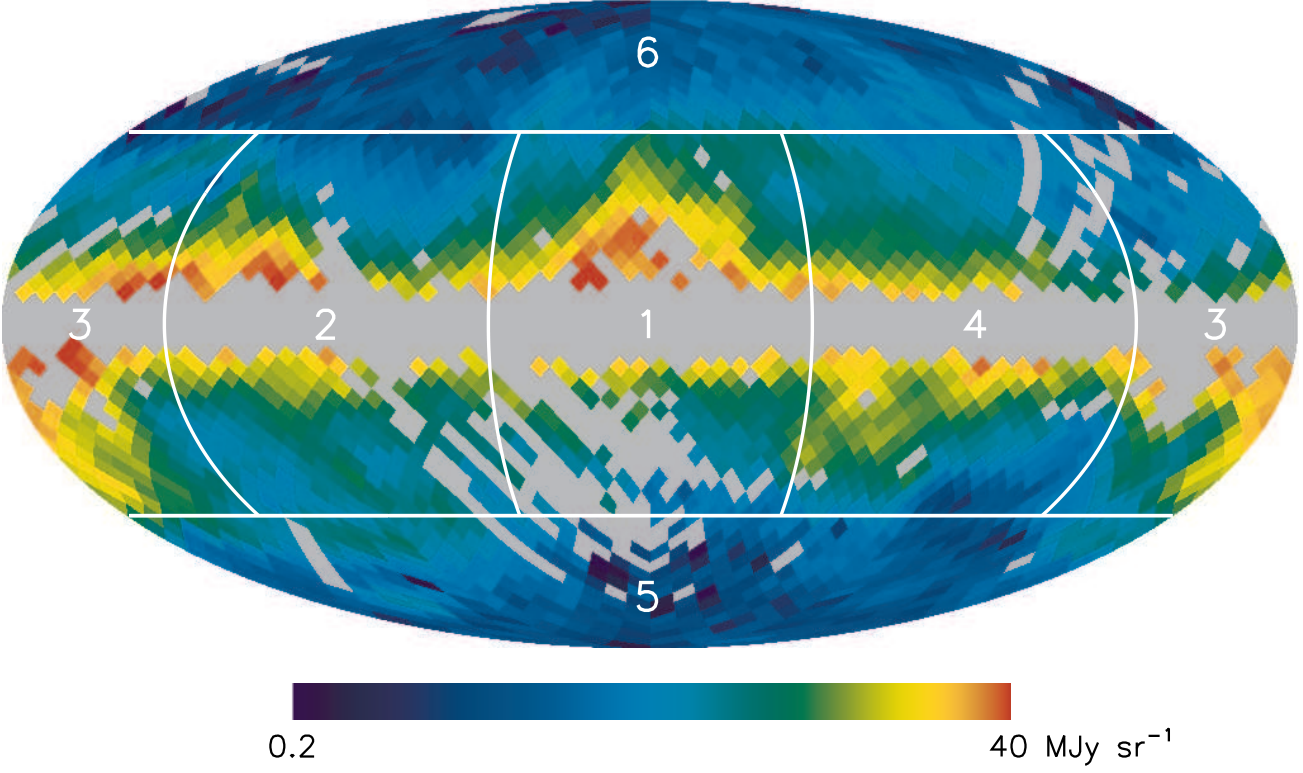


Figure 2. A map of Galactic dust emission from FIRAS observations averaged over seven channels centered at 1200 GHz ($250 \mu\text{m}$), on a logarithmic scale from 0.2 MJy sr^{-1} to 40 MJy sr^{-1} . Boundaries of the six large sky regions for which we form mean dust spectra are shown in white. FIRAS pixels inside of the mask of FDS appear gray and are excluded from our analysis. The mask excludes 29% of the sky.

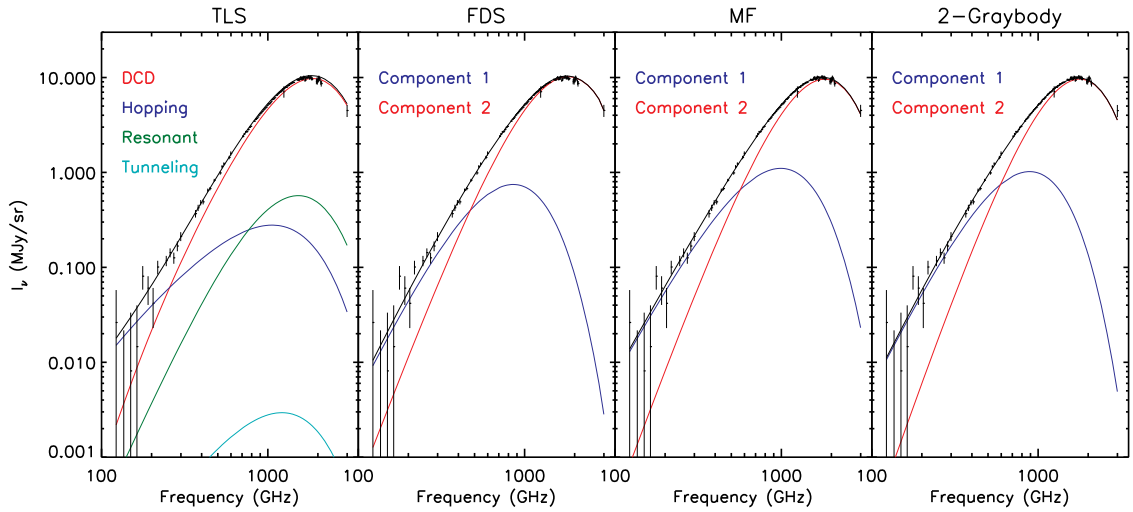


Figure 3. The Galactic dust spectrum formed from FIRAS and DIRBE data for the sky region centered at $l = 90, b = 0$, shown with results from fitting the two-level systems (TLS) model, FDS model, MF model, and two-graybody model. In each panel, the total model spectrum is shown as the black curve and individual model components are shown in color.

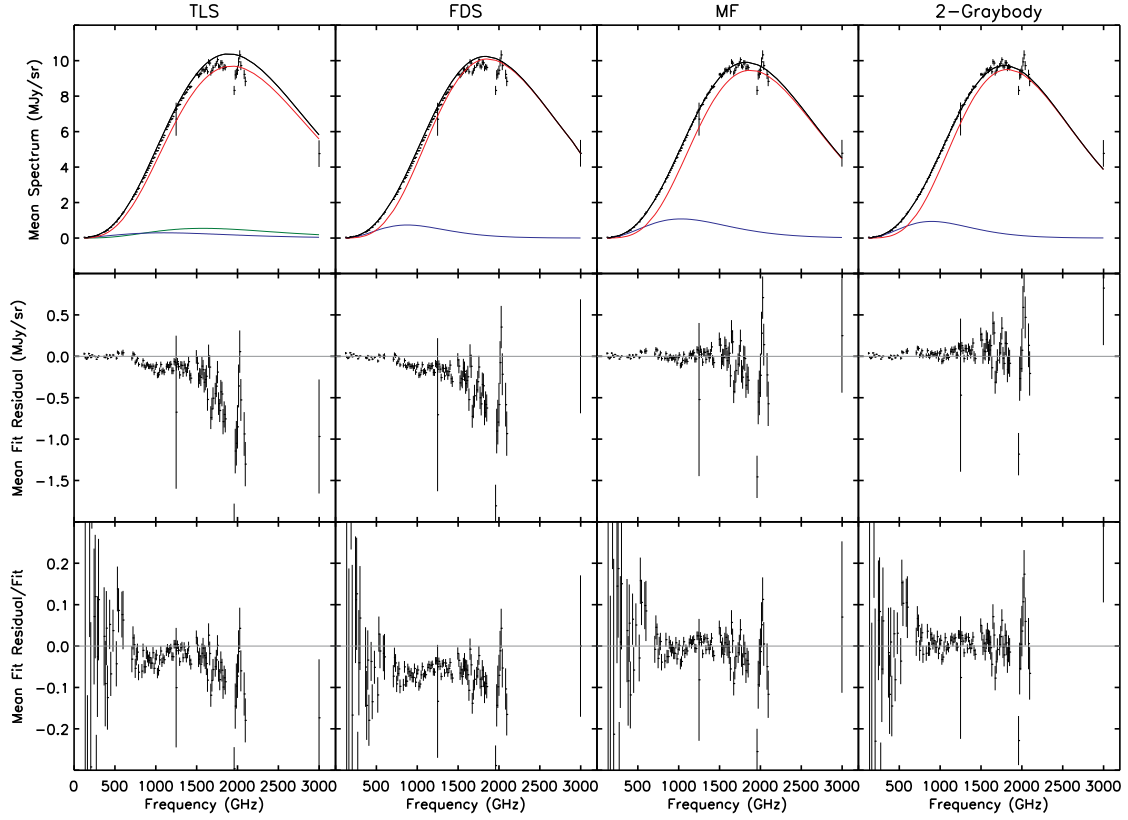


Figure 4. Averages over the full sky outside masked regions of Galactic dust spectra and model fits (top row), fit residuals (middle row), and fractional fit residuals (bottom row). Results are shown for the TLS model fit, FDS model fit, MF model fit, and two-graybody model fit. The color coding for the model components in the top row is the same as in Figure 3.

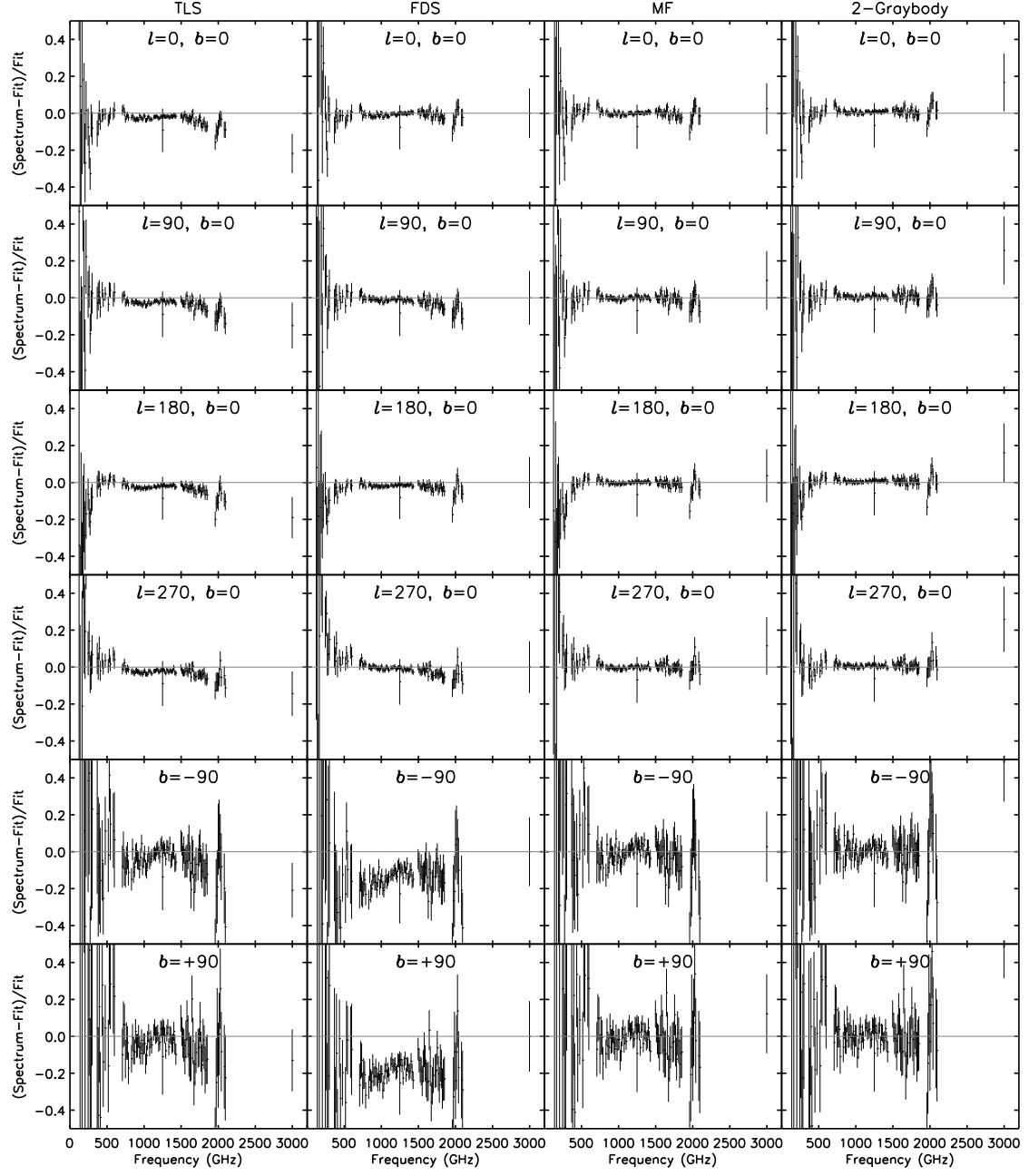


Figure 5. Fractional residuals of the dust model fits for each sky region. Results are shown for the TLS model fit, FDS model fit, MF model fit, and two-graybody model fit.

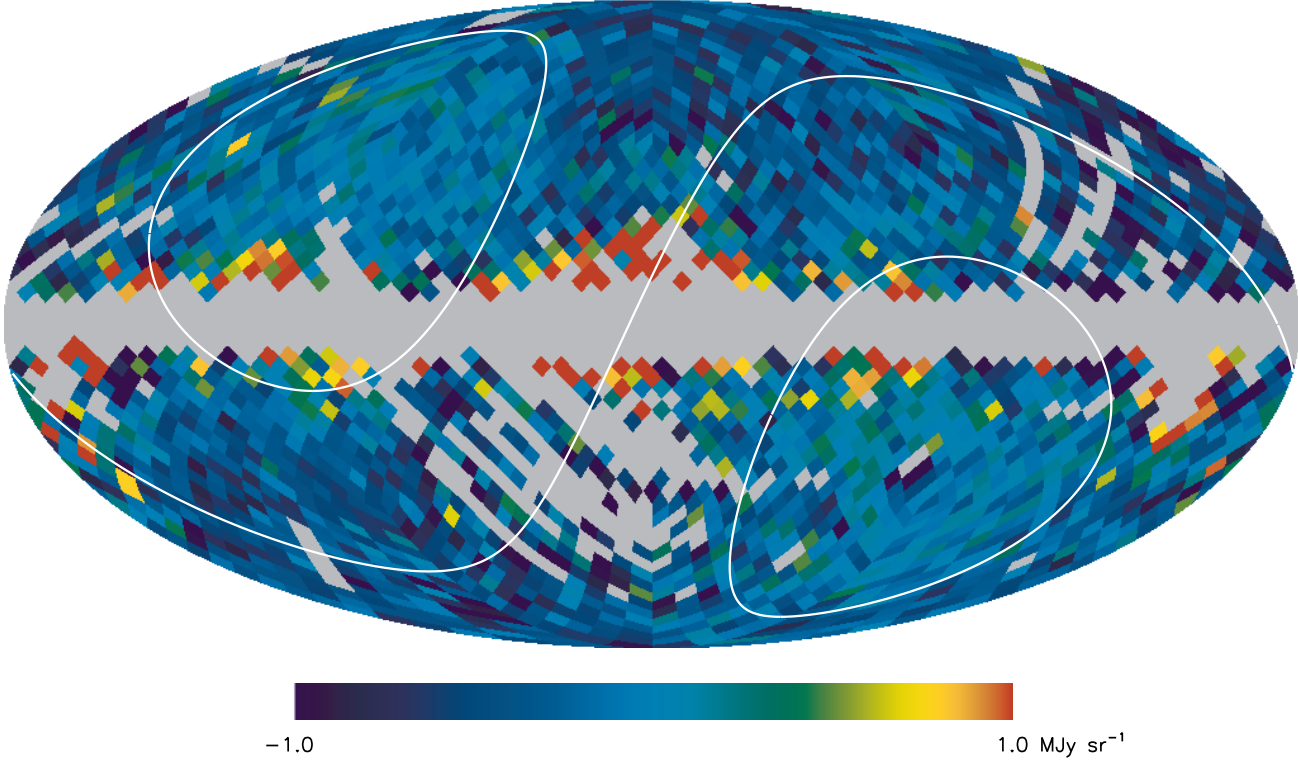


Figure 6. Residual of the FDS model fit calculated at FIRAS resolution, averaged over seven channels centered at 1200 GHz ($250 \mu\text{m}$), on a linear scale from -1 to 1 MJy sr^{-1} . Contours of ecliptic latitude equal to -45° , 0° , and $+45^\circ$ are shown in white. FIRAS pixels inside of the mask of FDS appear gray.

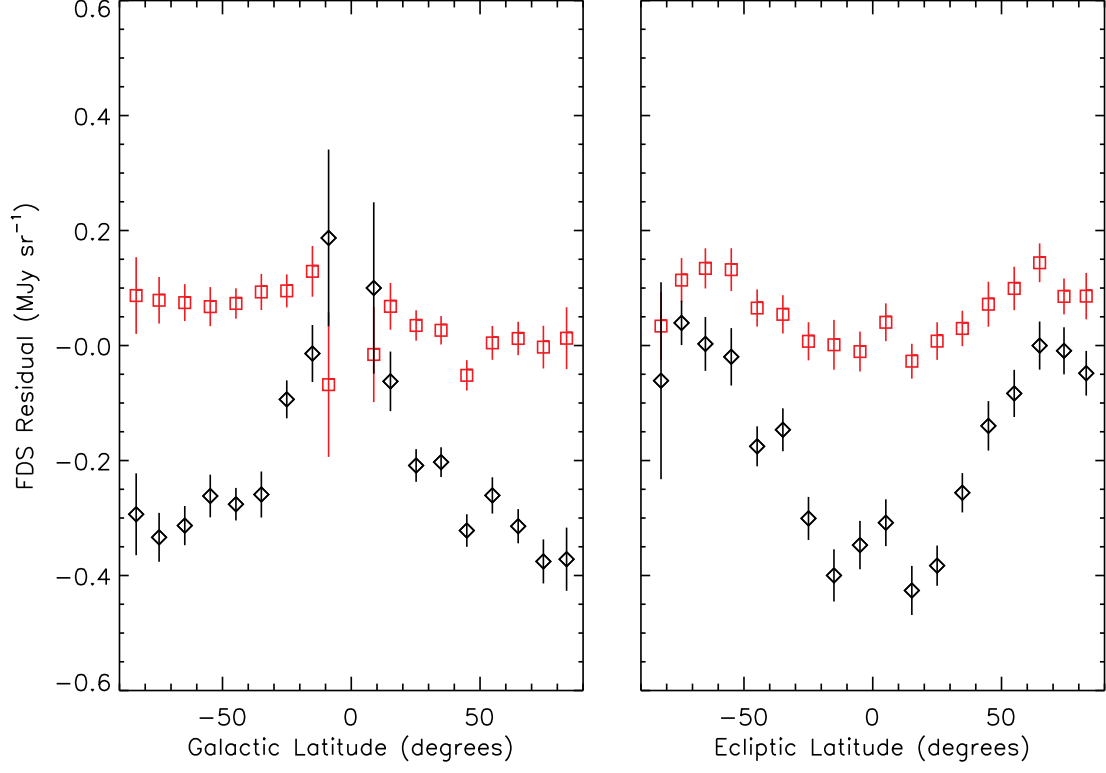


Figure 7. Dependence of the FDS fit residual at 1200 GHz on Galactic latitude and ecliptic latitude. The black diamonds show medians of the residual map shown in Figure 6 calculated over 10 degree bins in latitude. The red squares show results from fitting a modified version of the FDS model that uses a rescaled SFD $100\ \mu\text{m}$ map and a $100\ \mu\text{m}/240\ \mu\text{m}$ ratio map calculated from the *Planck* team thermal dust model.

Table 1
Dust Model Fit Parameters

Model	Global Parameters	Regional Parameters
TLS Model	Charge correlation length l_c Relative TLS amplitude A Tunneling states parameter c_Δ	Dust temperature T_d Spectrum amplitude a
FDS Model	Dust emissivity indices α_1, α_2 Component 1 fractional power f_1 Cross-section parameter q_1/q_2	None
MF Model	Dust emissivity indices α_1, α_2 Component 1 fractional power f_1 Cross-section parameter q_1/q_2	Dust temperatures T_2 Dust optical depths τ
2-Graybody Model	Warm dust emissivity index α_2	Dust temperatures T_1, T_2 Dust optical depths τ_1, τ_2

Table 2
Dust Model Fits

Model	Global Parameters	Fit χ^2	ν	$P(\chi^2 > \text{Fit } \chi^2)$	Fit χ_ν^2
TLS Model	$l_c = 15.6 \pm 7.8$ nm $A = 5.1 \pm 3.9$ $c_\Delta = 1510 \pm 1310$	690	663	0.231	1.04
FDS Model	$\alpha_1 = 1.69 \pm 0.10$ $\alpha_2 = 2.74 \pm 0.16$ $f_1 = 0.037 \pm 0.014$ $q_1/q_2 = 13.2 \pm 10.9$	2049	662 ^a	1.6×10^{-141}	3.10
MF Model	$\alpha_1 = 1.33 \pm 0.12$ $\alpha_2 = 2.91 \pm 0.45$ $f_1 = 0.070 \pm 0.073$ $q_1/q_2 = 11.0 \pm 13.7$	598	662	0.963	0.90
2-Graybody Model	$\alpha_1 = 1.7$ (fixed) $\alpha_2 = 3.20$	527	653	0.9998	0.81

^a The DIRBE 100 μm and 240 μm data points are not counted in the number of degrees of freedom for the FDS model fit because the model uses DIRBE 100 μm and 240 μm maps in its calculation of the dust spectrum for each region.

Table 3
Dust Model Regional Parameters

Model	χ_ν^2	Parameter	Region 1 (0, 0) ^a	Region 2 (90, 0)	Region 3 (180, 0)	Region 4 (270, 0)	Region 5 (0, -90)	Region 6 (0, 90)
TLS Model	1.04	T_{dust} (K) a (10^{-8} cm)	19.5 17	18.0 15	17.9 24	18.6 14	19.5 3.0	19.8 2.3
FDS Model ^b	3.10	T_1 (K) T_2 (K)	9.5 16.2	9.1 15.7	8.9 15.3	9.3 15.9	9.2 15.8	9.3 16.0
MF Model ^b	0.90	T_1 (K) T_2 (K) $\tau/10^{-5}$	12.1 15.8 13.7	11.1 14.9 12.2	11.1 14.8 19.8	11.5 15.3 12.0	12.1 15.9 2.5	12.4 16.1 1.8
2-Gray Model	0.81	T_1 (K) T_2 (K) $\tau_1/10^{-5}$ $\tau_2/10^{-5}$	9.6 14.7 15.3 10.0	9.2 13.8 12.5 8.8	9.5 13.9 18.4 13.5	9.0 14.2 14.9 8.7	6.5 13.7 7.4 2.8	6.7 14.0 5.9 2.0

^a Galactic coordinates (l, b) of the region center.

^b The dust temperatures T_1 and T_2 for the FDS model and T_1 for the MF model are derived parameters. All of the other parameters listed are fit parameters.